Hydroelastic response of floating elastic disks to regular waves. Part 2: Modal analysis

F. MONTIEL[1]†, L. G. BENNETTS[2], V. A. SQUIRE[1] F. BONNEFOY[3] AND P. FERRANT[3]

[1]Department of Mathematics and Statistics, University of Otago, P.O. Box 56, Dunedin 9054, New Zealand

[2]School of Mathematical Sciences, University of Adelaide, Adelaide, South Australia 5005, Australia

[3]Laboratoire de recherche en Hydrodynamique, Énergétique et Environnement Atmosphérique, École Centrale de Nantes, 1 rue de la Noë, Nantes, France

(Received 21 January 2013)

Validation of a linear numerical model of wave interactions with floating compliant disks is sought using data obtained from the wave basin experiments reported by Montiel *et al.* (submitted, submitted in parallel for publication in *J. Fluid Mech.*). Comparisons are made for both single-disk tests and the two-disk tests in which wave interactions between disks are observed. The deflection of the disk or disks is separated into the natural modes of vibration *in vacuo*. The decomposition allows the rigid-body motions and flexural motions to be analysed separately. Rigid-body motions are accurately replicated by the numerical model but, although passable agreement is found, the amplitudes of flexural modes are consistently overestimated. Extensions of the numerical model are used to discount the experimental configuration as a source of the discrepancies. An enhanced viscoelastic model for the disks is also proposed, which results in improved model/data agreement for the flexural motions but cannot account for all of the disagreement.

1. Introduction

In a companion paper Montiel *et al.* (2012*b*, hereinafter referred to as Part 1), a series of wave basin experiments are described. The aim of the experiments is to characterise the response of floating compliant disks to regular waves. The experiments are designed specifically to provide benchmark data for validation of the standard hydroelastic model (SHM) based on thin-elastic plate theory for the disks and the potential flow of an incompressible and inviscid fluid to describe the fluid motion. The model forms the kernel of theoretical research in the field of linear hydroelasticity.

Contemporary applications of the SHM are (i) the modelling of ocean waves/sea-ice interactions and (ii) the design of mat-like very large floating structures (VLFSs). Comprehensive accounts of the research in these two areas are reported in recent reviews by Squire (2007, 2011) for sea-ice, and Watanabe *et al.* (2004) and Chen *et al.* (2006) for VLFSs. Very few experimental studies to validate the SHM are reported by these authors, and they highlight the need for new investigations to remedy this important shortcoming.

We seek validation of the SHM for one and two compliant disks in a fluid domain of finite depth, and laterally unbounded, under the restrictions of the linear theory of water waves. In particular, our goal is to characterise the flexural motion of the disks under regular wave forcing. In Part 1 we described an experimental setup in a wave basin that

† Email address for correspondence: fmontiel@maths.otago.ac.nz

complies with the restrictions of the numerical model. We measured the deflection of the disks, for a range of thicknesses and wave forcings, and performed pointwise comparisons with the numerical model at a few isolated points. Good agreement was found for both the single- and two-disk tests datasets. The pointwise analysis gives little information on the flexural motion of the disks, however. In particular, the deflection of a disk is composed of rigid-body and flexural components, which need to be analysed separately to validate the SHM in the three-dimensional setting considered here.

In this paper, we propose an enhanced comparison analysis for the response of one and two disks. We use the decomposition of the vertical displacement of the circular thin-elastic plate into its natural modes of vibrations (NMV) *in vacuo* (Itao & Crandall 1979) to conduct our analysis. This decomposition separates the contribution due to the rigid-body modes (heave, pitch and roll) from that due to an infinite number of flexural modes. The amplitude associated with each mode provides a single quantity that can be estimated numerically by integration over the surface of the disk from the theoretical and experimental deflection data. Comparing these quantities then provides trends of agreement and discrepancy for the rigid-body and flexural motions separately.

Preliminary analyses conducted in Part 1 suggest that the numerical model tends to overestimate the bending motion in the disk or disks compared to that measured experimentally. A theoretical analysis is conducted here to determine if the discrepancy in flexural motion is due to the experimental setup described below. We also consider a new plate model that includes viscoelastic effects to introduce frequency-dependent damping in the motion of the disks.

The SHM consists of a collection of floating thin-elastic disks (Love 1944). Under time-harmonic linear wave forcing, the disks respond freely in the vertical direction but a restriction is imposed on the in-plane rigid-body motions (surge, sway and yaw). We extend previous solutions to the single-disk problem (see Meylan & Squire 1996; Peter *et al.* 2003; Andrianov & Hermans 2005), as we consider the effect of Archimedean draught on the response. Application of Graf's interaction theory (Kagemoto & Yue 1986) is used for the multiple-disk problem.

In order to reproduce experimentally the conditions of the SHM, we implemented a number of innovative technical solutions in the setup. We used disks of radius 0.72 m and made of expanded PVC to test the validity of thin-elastic plate model. Preliminary bending tests were conducted to measure the Young's modulus of the material. To restrict the in-plane rigid-body motions, we constructed an anti-motion device comprising two vertical aluminium rods respectively passing through the disk at its centre (central rod) and close to an edge (edge rod). The disks were also equipped with an edge barrier stuck along their circular contour to prevent flooding events.

Measurements of the deflection of the disks were performed with a remote sensing motion tracking device. We were able to reconstruct the motion of each disk using displacement data obtained at 78 points. Single-disk tests were carried out for three thicknesses (3, 5 and 10 mm), two incident wave steepnesses ($\varepsilon = 2A/\lambda = 1$ and 2%, where A is the incident wave amplitude and λ is the wavelength) and eight frequencies (distributed evenly over the range 0.6–1.3 Hz). We also conducted tests with two disks for two thicknesses (3 and 10 mm), one steepness (1%) and four arrangements, over the same frequency range. To the authors' knowledge, this is the first attempt to test the validity of the SHM in three dimensions.

An appropriate data processing technique was devised in Part 1 to extract the linear time-harmonic component of the raw time series, that complies with the conditions of application of the SHM. The method is a discrete version of the short-time Fourier transform (STFT; see, e.g., Allen & Rabiner 1977; Cohen 1989), which generates the

time evolution of each Fourier component. Truncating the first-order component in a relevant steady-state window provides the processed data. In the present paper, we use the STFT method to generate the experimental modal amplitudes associated with the NMV of the disks.

To justify the discrepancies in the flexural motion observed in the comparisons, we analyse the effects of a number of components from the experimental setup by extending the original numerical model. In particular, we discuss the effect of the central rod on the motion and conduct a theoretical analysis to determine if the edge barrier affects the flexural motion of the disk.

A brief description of the numerical model and solution method is given in §2. The NMV of the disk *in vacuo* and the corresponding modal expansion for its deflection is introduced in §3. A model/experiment comparative analysis for the single-disk tests is then conducted on the modal amplitudes associated with the rigid-body modes and a relevant set of flexural modes. After identifying the trends of agreement and discrepancy, a list of potential sources of discrepancy is given. In §4, we model the influence of the edge barrier on the response of the disk to validate the experimental procedure. Based on a preliminary analysis showing the sensitivity of modal amplitude spectra to variations of the Young's modulus, an extension to the SHM is proposed in §5 to account for damping effects in the bending motion of the disk. A viscoelastic model is derived and calibrated using the data from the bending tests that were conducted to measure the Young's modulus of the disks. The improvements of this approach compared to the SHM are then examined. In §6, a model/experiment comparative analysis is conducted for the two-disk tests. A summary of the main findings of the analysis is given in §7.

The investigation described in this paper is part of a PhD project, and is reported in full detail by Montiel (2012).

2. Model of wave scattering by a floating elastic disk

Consider a compliant disk of thickness D and radius R floating freely on a fluid domain Ω, which is of constant depth h and unrestricted in the horizontal directions. Let $\mathbf{x} = (r, \theta, z)$ denote the cylindrical coordinates of a point in the fluid. The vertical coordinate is $z \in (h, 0)$, which points upwards and has its origin located at the undisturbed free surface. The horizontal plane is described by the radial coordinate $r > 0$ and the azimuthal coordinate $\theta \in (-\pi, \pi]$. The origin of the radial coordinate r is the disk's centre, and that of the azimuthal coordinate θ is aligned with the direction of the incident wave. From Archimedes' principle, the draught of the disk at rest is given by $d = (\rho/\rho_0)D$, where ρ is the density of the disk and $\rho_0 \approx 1000\,\mathrm{kg\,m^{-3}}$ is the density of the fluid. From the measurements reported in Part 1, we have $\rho \approx 623$, 547 and $530\,\mathrm{kg\,m^{-3}}$ for $D = 3$, 5 and 10 mm, respectively.

Under the standard assumptions of linear water-wave theory and time-harmonic motions (with radian frequency ω), we describe the fluid motion using the velocity potential $\Phi(\mathbf{x}, t) = \mathrm{Re}\{\phi(\mathbf{x})\,\mathrm{e}^{\mathrm{i}\omega t}\}$. The (reduced) potential ϕ is complex-valued. It satisfies Laplace's equation throughout the fluid and a no-flow condition on the bed, i.e.

$$\nabla^2\phi + \partial_z^2\phi = 0 \quad (\mathbf{x} \in \Omega) \quad \text{and} \quad \partial_z\phi = 0 \quad (z = -h), \tag{2.1}$$

where ∇^2 denotes the Laplace operator in polar coordinates, i.e. $\nabla^2 = \partial_r^2 + (1/r)\partial_r + (1/r^2)\partial_\theta^2$. On the mean free surface, the linearised condition

$$\partial_z\phi = \alpha\phi \quad (r > R,\, z = 0) \tag{2.2}$$

applies, where $\alpha = \omega^2/g$ is a frequency parameter and $g \approx 9.81\,\mathrm{m\,s^{-2}}$ is acceleration due to gravity.

We describe the vertical deformations of the disk using thin-elastic plate theory (Love 1944), which assumes a small aspect ratio ($D/2R \ll 1$) and that the deformation remains small compared to the thickness. The elastic behaviour is characterised by two constants, the Young's modulus E and Poisson's ratio $\nu \approx 0.3$. Allowing the disk to move freely in the vertical direction, we obtain a condition for ϕ on the disk's underside, given by

$$\left(\beta\nabla^4 + 1 - \alpha d\right)\partial_z\phi = -\alpha\phi \quad (z = -d) \tag{2.3}$$

where $\beta = F/\rho_0 g$, with $F = ED^3/12(1-\nu^2)$ the flexural rigidity. In addition, free-edge conditions apply. These are

$$\left[r^2\nabla^2 - (1-\nu)\left(r\partial_r + \partial_\theta^2\right)\right]\partial_z\phi = 0 \quad (r = R), \tag{2.4a}$$

and

$$\left[r^3\partial_r\nabla^2 + (1-\nu)\left(r\partial_r - 1\right)\partial_\theta^2\right]\partial_z\phi = 0 \quad (r = R), \tag{2.4b}$$

which represent, respectively, vanishing of bending moment and shearing stress. We also assume that the motions in the horizontal directions are restricted, so that

$$\partial_r\phi = 0 \quad (r = R,\ -d \le z \le 0). \tag{2.5}$$

We express the solution of the boundary value problem using eigenfunction expansions. In the free-surface region ($r > R$), the potential is denoted by $\phi^{(\mathrm{o})} = \phi_I + \phi_S$, and is composed of a prescribed harmonic forcing term $\phi_I(\mathbf{x}) = (\,\mathrm{i}g/\omega)\exp(k_0 r\cos\theta)\cos k_0(z+h)/\cos k_0 h$ with unit amplitude (travelling in the direction $\theta = 0$ towards $\theta = \pi$) and an as yet unknown scattered wave component $\phi_S(\mathbf{x})$. In the far field ($r \to \infty$), the scattered wave decay is governed by the Sommerfeld radiation condition

$$r^{1/2}\left(\partial_r + k_0\right)\phi_S \to 0, \tag{2.6}$$

where the wavenumber k_0 will be defined shortly. The eigenfunction expansion is then given by the truncated series

$$\phi_S(\mathbf{x}) \approx \sum_{m=0}^{M} \varphi_m^{(\mathrm{o})}(z) \sum_{n=-N}^{N} A_{m,n}^{(\mathrm{o})} \mathrm{K}_n(k_m r)\,\mathrm{e}^{\,\mathrm{i}n\theta} \quad (r > R), \tag{2.7}$$

where $A_{m,n}^{(\mathrm{o})}$ ($m = 0,\ldots,M$, $n = -N,\ldots,N$) represent unknown amplitudes and K_n denotes the modified Bessel function of the second kind of order n. We have also introduced the vertical modes $\varphi_m^{(\mathrm{o})}(z) = \cos k_m(z+h)$, $0 \le m \le M$, where the quantities k_m are roots the dispersion relation

$$k\tan kh = -\alpha, \tag{2.8}$$

such that k_0 is purely imaginary and k_m, $m \ge 1$, are real and ordered in ascending magnitude. In (2.7), the wave-like component associated with k_0 supports a travelling wave that decays geometrically as $\mathrm{O}\left(r^{-1/2}\right)$, while those associated with k_m, $m \ge 1$, support evanescent waves, which decay exponentially with distance away from the edge of the disk. Numerical evidence indicates that as k_m increases, the contribution of the corresponding eigenfunctions in (2.7) diminishes, which justifies the truncation in (2.7).

In the disk-covered fluid domain, the eigenfunction expansion of the potential, denoted by $\phi^{(\mathrm{i})}$, takes the form

$$\phi^{(\mathrm{i})}(\mathbf{x}) \approx \sum_{p=-2}^{M} \varphi_p^{(\mathrm{i})}(z) \sum_{n=-N}^{N} A_{p,n}^{(\mathrm{i})} \mathrm{I}_n(\kappa_p r)\,\mathrm{e}^{\,\mathrm{i}n\theta} \quad (r < R), \tag{2.9}$$

where $A^{(\mathrm{i})}_{p,n}$ ($p=-2,\ldots,M$, $n=-N,\ldots,N$) are the unknown amplitudes, and I_n ($n=-N,\ldots,N$) are the modified Bessel functions of the first kind of order n. The vertical modes are $\varphi^{(\mathrm{i})}_p(z)=\cos\kappa_p(z+h)$, $-2\le p\le M$, such that κ_p are roots of the dispersion relation

$$\left(\beta\kappa^4+1-\alpha d\right)\kappa\tan\kappa\,(h-d)=-\alpha. \tag{2.10}$$

Similarly to the free-surface dispersion relation (2.8), κ_0 is purely imaginary and is associated with a travelling wave component, and κ_p, $1\le p\le M$, are real and ordered in ascending, and define vertical modes that support evanescent waves. The dispersion relation (2.10) also admits two typically complex roots labelled κ_{-2} and κ_{-1}, which support damped travelling waves (Bennetts 2007). Thus, two additional modes are present in comparison to the solution in the free-surface region.

We devise a version of the eigenfunction matching method (EMM) to solve for the unknown amplitudes. This technique is based on enforcing weak continuity of fluid pressure and velocity at the interface between free-surface and disk-covered fluid regions. Our solution extends the two-dimensional EMM of Montiel *et al.* (2012*a*). The EMM is an efficient method to obtain two to three significant digit accuracy (Kohout *et al.* 2007), which is sufficient for comparison with experimental data. It is also suitable for the model enhancements made in §4 and §5.

To implement the EMM, let u describe the normal velocity at the interface between the free-surface and disk-covered fluid domains ($r=R$). Using angular periodicity, we decompose u in its Fourier modes as $u(\theta,z)=\sum_{n=-\infty}^{n=\infty}u_n(z)\,\mathrm{e}^{\mathrm{i}n\theta}$. Invoking continuity of fluid pressure and velocity throughout the fluid, the matching equations are given by

$$\phi^{(\mathrm{o})}(\mathbf{x})=\phi^{(\mathrm{i})}(\mathbf{x}),\quad \partial_r\phi^{(\mathrm{o})}(\mathbf{x})=u(\theta,z)=\partial_r\phi^{(\mathrm{i})}(\mathbf{x})\quad (r=R,\,-h\le z<-d). \tag{2.11}$$

Using the linear independence of the Fourier basis in the matching equations (2.11), yields a set of one-dimensional matching equations involving the functions $u_n(z)$. To implement the numerical procedure, we approximate $u_n(z)$ as a partial expansion of $Q+1$ weighted Gegenbauer polynomials $u^q_n(z)$, which dictate the asymptotic behaviour of the velocity in the vicinity of the submerged corner (Williams & Porter 2009). Montiel (2012) proposed a detailed analysis of the convergence properties of this expansion.

A system of equations for the unknown amplitudes $A^{(\mathrm{o})}_{m,n}$ and $A^{(\mathrm{i})}_{p,n}$ is obtained by projecting the matching equations (2.11) onto spaces spanned by the different vertical modes. Using (2.5), we obtain

$$\sum_{m=0}^{M}k_mA^{(\mathrm{o})}_{m,n}\mathrm{K}_n^{'}(k_mR)\int_{-h}^{0}\varphi^{(\mathrm{o})}_m(z)\varphi^{(\mathrm{o})}_r(z)\,\mathrm{d}z\approx\int_{-h}^{-d}u_n(z)\varphi^{(\mathrm{o})}_r(z)\,\mathrm{d}z, \tag{2.12a}$$

$r=0,\ldots,M$, and

$$\sum_{p=-2}^{M}\kappa_pA^{(\mathrm{i})}_{p,n}\mathrm{I}_n^{'}(\kappa_pr)\int_{-h}^{0}\varphi^{(\mathrm{i})}_p(z)\varphi^{(\mathrm{i})}_s(z)\,\mathrm{d}z\approx\int_{-h}^{-d}u_n(z)\varphi^{(\mathrm{i})}_s(z)\,\mathrm{d}z, \tag{2.12b}$$

$s=-2,\ldots,M$, for the continuity of fluid velocity. In the last two equations, the prime superscript denotes the derivative. Continuity of the fluid pressure is given by

$$\sum_{m=0}^{M}A^{(\mathrm{o})}_{m,n}\mathrm{K}_n(k_mR)\int_{-h}^{-d}\varphi^{(\mathrm{o})}_m(z)u^q_n(z)\,\mathrm{d}z\approx\sum_{p=-2}^{M}A^{(\mathrm{i})}_{p,n}\mathrm{I}_n(\kappa_pR)\int_{-h}^{-d}\varphi^{(\mathrm{i})}_p(z)u^q_n(z)\,\mathrm{d}z, \tag{2.12c}$$

$0\le q\le Q$. Note that the modes $\varphi^{(\mathrm{o})}_m(z)$ are orthogonal, but the modes $\varphi^{(\mathrm{i})}_p(z)$ are not.

Equations (2.12) define a system of $2M+Q+3$ equations for each Fourier component. Applying the edge conditions (2.4) completes the system. Algebraic manipulations, similar to those described in Montiel *et al.* (2012*a*), are used to obtain the solution.

The deflection of the disk, $\eta(r,\theta,t) = \mathrm{Re}\{w(r,\theta)\,\mathrm{e}^{\,\mathrm{i}\omega t}\}$, is obtained from the kinematic condition $w = (1/\,\mathrm{i}\omega)\partial_z\phi^{(\mathrm{i})}$ at $z=-d$. This gives

$$w(r,\theta) \approx (1/\,\mathrm{i}\omega)\sum_{p=-2}^{M}\varphi_p^{(\mathrm{i})'}(-d)\sum_{n=-N}^{N}A_{p,n}^{(\mathrm{i})}\mathrm{I}_n(\kappa_p r)\,\mathrm{e}^{\,\mathrm{i}n\theta} \quad (r<R). \tag{2.13}$$

3. Modal analysis of a single disk

3.1. *Natural modes expansion*

We will compare theoretical and experimental data for integrated quantities over the disk's surface as a means to characterise the response of the disk. We decompose the motion of the disk into the natural modes of vibration (NMV) of the disk *in vacuo*, denoted by $w_{n,j}(r,\theta)$, $n\in\mathbb{Z}$, $j\in\mathbb{N}$. A derivation of the NMV, also commonly referred to as the dry modes in ship hydroelasticity, is given in Meylan & Squire (1996). The NMV are orthogonal with respect to the inner-product

$$\langle f_1, f_2\rangle = \int_0^R\int_0^{2\pi} f_1(r,\theta)f_2(r,\theta)r\,\mathrm{d}r\,\mathrm{d}\theta.$$

The deflection of the disk may therefore be represented as a superposition of the NMV with corresponding amplitudes $A_{n,j}$, i.e.

$$w(r,\theta) = \sum_{n=-\infty}^{\infty}\sum_{j=0}^{\infty}A_{n,j}w_{n,j}(r,\theta), \quad A_{n,j} = \frac{\langle w, w_{n,j}\rangle}{\langle w_{n,j}, w_{n,j}\rangle}, \tag{3.1}$$

$n\in\mathbb{Z}$, $j\in\mathbb{N}$.

The advantage of decomposing the deflection of the disk into the NMV is that it separates the rigid-body and flexural motions. Heave, roll and pitch are the rigid-body modes, denoted by $w_{0,0}$, $w_{-1,0}$ and $w_{1,0}$, respectively. In contrast, in the eigenfunction decomposition (2.13), each mode consists of rigid-body and flexural components. Also note that the NMV are separated into symmetric and anti-symmetric modes (with respect to $\theta=0$, π), corresponding to $n\geq 0$ and $n<0$, respectively. This reduces our analysis to evaluating the modal amplitudes $A_{n,j}$ for $n\geq 0$ for symmetric problems.

We consider a subset of eight modal amplitudes $A_{n,j}$ for the comparison analysis, corresponding to the modes being the most excited, later referred to as dominant modes. These are $A_{n,0}$, $n=0$–4, and $A_{n,1}$, $n=0$–2. Preliminary analyses showed that higher-order NMV undergo very little excitation in our parameter range. Figure 1 shows the mode shape of the dominant modes. Surfaces are shown for a disk of unit radius, without loss of generality. Note that the angular and radial indexes (n and j) represent the number of nodal diameters and nodal circles of the NMV, respectively.

The experimental deflection data are obtained by interpolation of the displacement data from 78 points of the disk surface, while the theoretical deflection is calculated from (2.13). Standard integration techniques are used to evaluate the amplitudes. The results provided in this paper are given with an accuracy of at least two decimal places for a unit wave forcing.

Using the experimental measurements, we generate a time series for each modal amplitude, which is then processed using the short-time Fourier transform (STFT) method

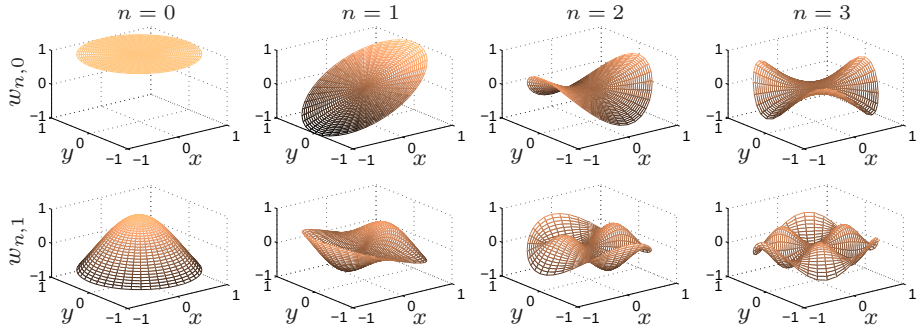

FIGURE 1. Diagram of the mode shape of eight symmetric NMV $w_{n,j}$, $n = 0$–3, $j = 0$, 1.

described in Part 1. The method provides the time evolution of each Fourier component of the signal. We then take the mean of the fundamental amplitude in a relevant steady-state time-window, which removes the influence of the transient regime and the wave basin lateral boundaries. Therefore, we obtain the linear time-harmonic amplitude associated with the time series, which can be compared with the model's prediction. Additional details regarding the experimental setup and the STFT method are given in Part 1 (§4.1).

The STFT processing technique generates a single value for each test and mode, therefore allowing us to analyse the modal amplitudes over the frequency range of interest $f = 0.5$–$1.5\,\mathrm{Hz}$. In addition, we remove the dependence of the results due to the incident wave amplitude, A say, as we use the conventional scalings $\tilde{A}_{n,j} = A_{n,j}/A$, for all $(n, j) \neq (1, 0)$, and $\tilde{A}_{1,0} = A_{1,0}/|k_0|A$, where k_0 is defined in §2. Subsequently, frequency-dependent scaled modal amplitudes are referred to as response amplitude operators (RAOs).

3.2. *Comparison model/experiments*

Figure 2 shows the scaled rigid-body RAOs, i.e. heave and pitch, for the three disk thicknesses considered, $D = 3$, 5 and 10 mm. We use a logarithmic scale to facilitate the readings for low magnitude responses. Each experimental amplitude is defined as the mean value of four repeated tests and the error bars correspond to the standard deviation (see Part 1 for more information about the tests conducted).

The experimental and theoretical RAOs display good agreement, with a relative difference (at each experimental frequency) of 5–20%. The only significant differences are found in the vicinity of the phase change in heave predicted by the model for the 3 and 5 mm disks (see panels a and b, respectively). This feature is not present in the experimental RAOs, although we would need to conduct additional tests using a denser frequency sampling to give conclusive statements. Away from these frequencies, the numerical model slightly overestimates the measured response. It is seen that the error bars are small for these modes (relative standard deviation of 5–10%) except at a few isolated frequencies, suggesting good repeatability of the tests. At $f = 0.6\,\mathrm{Hz}$, we observe that the discrepancy between theoretical and experimental RAOs is larger for the pitch mode ($\approx 20\%$ pointwise relative difference), consistently for the three thicknesses. In §3.3, we will list possible drivers of the discrepancies observed.

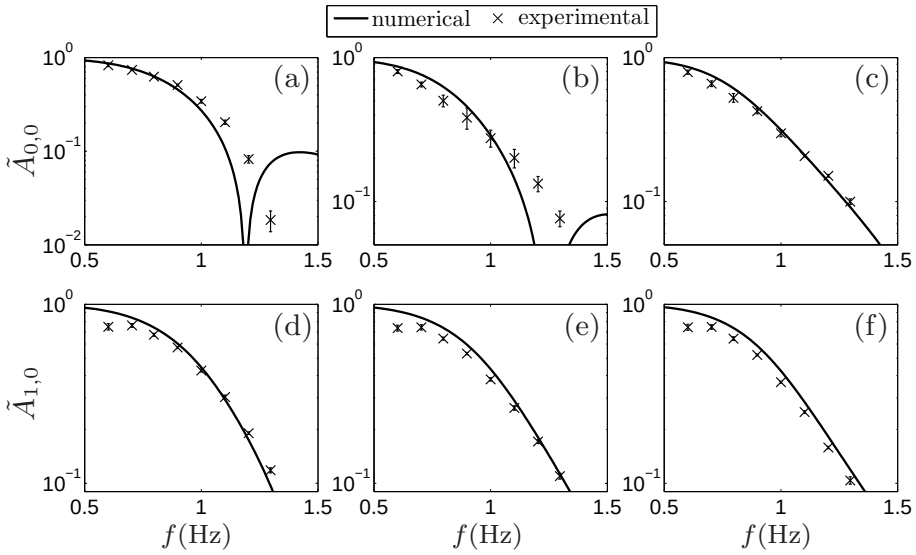

FIGURE 2. Model/experiment comparisons of the scaled RAOs in (a–c) heave $\tilde{A}_{0,0}$ and (d–f) pitch $\tilde{A}_{1,0}$. The RAOs are given for disk thicknesses (a,d) $D = 3\,\text{mm}$, (b,e) $D = 5\,\text{mm}$ and (c,f) $D = 10\,\text{mm}$.

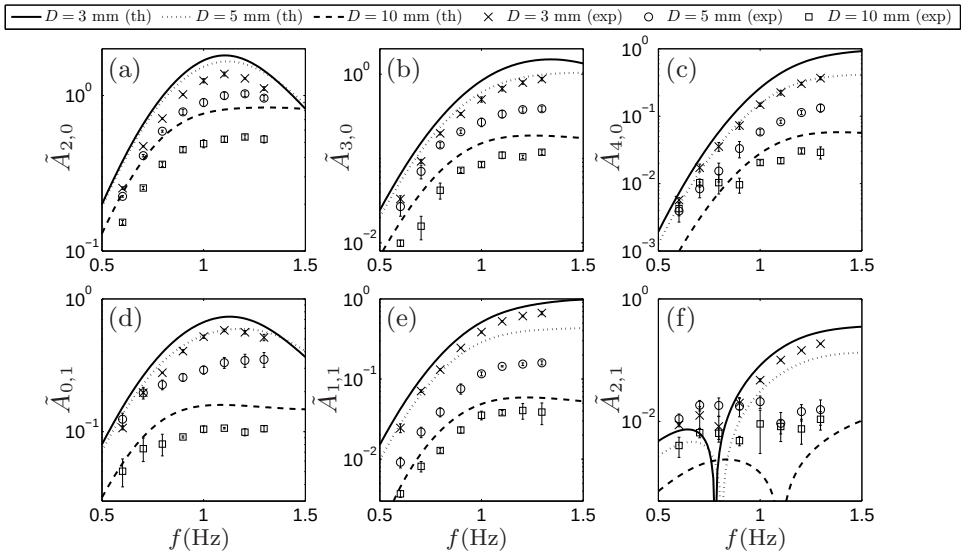

FIGURE 3. Model/experiment comparisons of the flexural modes RAOs (a) $\tilde{A}_{2,0}$, (b) $\tilde{A}_{3,0}$, (c) $\tilde{A}_{4,0}$, (d) $\tilde{A}_{0,1}$, (e) $\tilde{A}_{1,1}$ and (f) $\tilde{A}_{2,1}$. For each mode, the theoretical and experimental RAOs are given for disk thicknesses $D = 3\,\text{mm}$ (solid lines and crosses), $D = 5\,\text{mm}$ (dotted lines and circles) and $D = 10\,\text{mm}$ (dashed lines and squares).

The RAOs associated with the six dominant flexural modes are shown in figure 3. The agreement between numerical predictions and experimental data is not as good for the flexural modes as for the rigid-body modes. However, we note that the frequencies at which resonance peaks are observed for $\tilde{A}_{2,0}$ and $\tilde{A}_{0,1}$, are consistent between numerical model and experiments. The numerical model overestimates the experimental amplitudes of the flexural modes in all cases, except for low amplitude responses (e.g. $\tilde{A}_{2,1}$ at low frequencies for all thicknesses and at high frequencies for $D = 10\,\text{mm}$) due to the limited resolution of the measuring device. For the other modes, we find a relative difference of 30–70% overall for the three disks considered, away from the frequencies associated with significant discrepancies (e.g. phase changes or very low theoretical amplitudes). The agreement is better for the 3 and 10 mm disks (30–50% relative difference) than for the 5 mm disk (40–70% relative difference). The relative difference is higher than that estimated for the rigid-body modes and does not depend strongly on the frequency. We observe that all occurrences of significant discrepancy between theoretical and experimental data (e.g. panel c for $D = 10\,\text{mm}$ and panel f for $D = 5$ and 10 mm) correspond to RAOs with magnitudes less than 0.01. This relates to dimensional modal amplitudes of less than 1% of the incident wave amplitude, for which the accuracy is limited by the resolution of the measuring device. Such small amplitudes contribute very little to the motion of the disk and are not discussed further in this paper.

3.3. *Possible sources of discrepancy*

Although pointwise model/data comparisons of disk deflections showed a good overall agreement (see Part 1), discrepancies have been found in the more rigorous comparison of RAOs. In particular, the numerical model consistently overestimates the flexural response by at least 30%, suggesting that additional physical processes have been neglected in the model.

A number of phenomena can be discarded straightforwardly as major sources of discrepancy. In particular, theoretical analyses conducted by Fox & Squire (1991) and Balmforth & Craster (1999) on semi-infinite plates have shown that the effect of rotary inertia and shear distortion are negligible in a regime similar to that considered here. Therefore, it is reasonable to conclude that these effects are irrelevant in our experiments. In addition, the validity of the inviscid fluid approximation is deduced from the order of magnitude of the two non-dimensional quantities $kR \geq \mathrm{O}(1)$ and $A/R \ll 1$, where k is the wavenumber of the incident wave. These validate the large body approximation and allow us to discard form drag. Additional frictional sources arising from fluid/structure interaction, such as skin friction are neglected, based on previous observations that form drag dominates skin friction in similar situations (Kohout *et al.* 2011).

A pointwise analysis of non-linearities in the motion was conducted in Part 1. It was found that the amplitudes of the second–order harmonics are less than 5% of the fundamental amplitude in most cases, and that similar non-linearities inherent to the incident wave explain this behaviour in the disk's motion. We expect to find similar non-linear effects in the experimental RAOs when the magnitude of the fundamental amplitude is sufficiently high to be captured accurately by the measuring device. On the other hand, the limited resolution of the measuring device does not provide accurate measurements in regimes characterised by RAOs of very low magnitude, e.g. $\mathrm{O}\left(10^{-5}\right)$ m. In these cases, experimental noise has the same order of magnitude as that of the amplitude, so that the proportion of higher-order harmonics compared to the fundamental component increases.

We illustrate these assertions for the RAOs $\tilde{A}_{2,0}$ and $\tilde{A}_{3,0}$. We define the relative harmonic amplitude $\tilde{A}^{(2)}_{n,0}$ (expressed in percent), $n = 2,\ 3$, as the ratio of the second-order amplitude to the fundamental amplitude. Figure 4 shows the relative second-order RAOs,

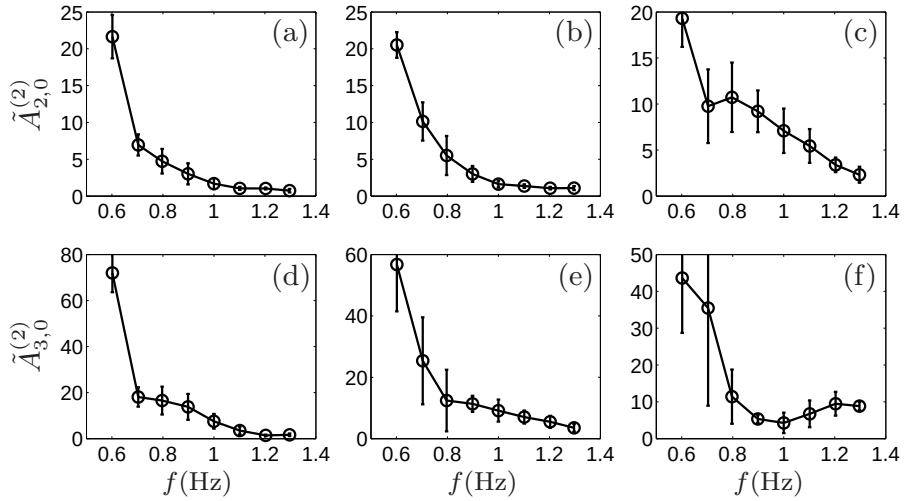

FIGURE 4. Relative second-order RAOs of (a–c) $\tilde{A}_{2,0}$ and (d–f) $\tilde{A}_{3,0}$ (in percents). Panels (a,d), (b,e) and (c,f) show the RAOs associated with $D = 3$, 5 and 10 mm, respectively.

for each disk thickness. Each data point is defined as the mean over four repeated tests, similarly to the fundamental amplitudes analysed in §3.2, and error bars are included. As expected, we observe that the proportion of second-order components increases at low frequencies consistently for all the thicknesses and both NMV. In the low frequency regime, the NMV have very low magnitude, as shown in figure 3, and contribute very little to the motion of the disk. Experimental noise due to the limited resolution of the measuring device is likely to explain this behaviour. In the mid- to high-frequency range, we find relative harmonic amplitude of less than 10%, which can be attributed to non-linearities in the incident wave or arising from scattering at the disk edge. These higher-order components are filtered as part of the data processing method. Therefore, we do not consider the influence of non-linear effects further in this paper, keeping in mind that in regimes characterised by RAOs of very low magnitude (low frequencies for the dominant flexural modes and pitch, and high frequencies for heave), non-linearities are probably a major source of discrepancy due to experimental noise of the same order of magnitude as the fundamental amplitude.

The experimental setup does not restrict the anti-symmetric motion in the disk. Although the forcing is applied symmetrically, imperfections in the setup may cause anti-symmetric modes to be slightly excited. Unfortunately, we have no means of quantifying the magnitude of the anti-symmetric NMV for the single disk case, as we have measured the displacement on half the disk only. However, we have validated the symmetry assumption pointwise for a few test cases (see Montiel 2012), suggesting that anti-symmetric modes experience negligible excitation.

We now consider the influence of the central rod restricting partially the disk's horizontal motion on the response of the disk. An extension of the SHM that accounts for surge and sway has been devised by Montiel (2012) to estimate the effect of the residual horizontal motion. The analysis concluded that the effect on the rigid-body and flexural modes is insignificant. Montiel (2012) also proposed a numerical model to include fric-

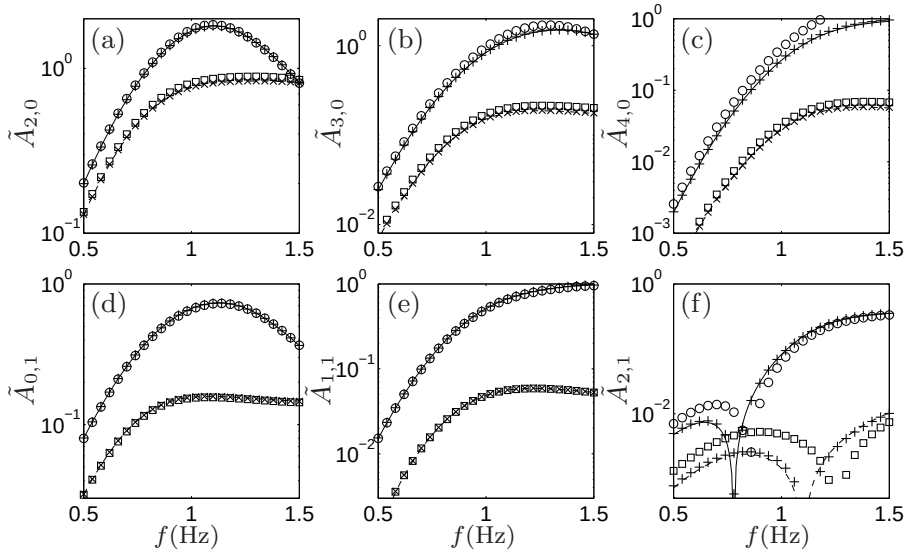

FIGURE 5. Influence of the edge beam on the flexural modes. The theoretical RAOs are given for the free edge case (solid and dashed line), and for an edge beam with Young's modulus $E_b = 1\,\mathrm{MPa}$ (pluses and crosses) and $E_b = 10\,\mathrm{MPa}$ (circles and squares), for two disk thicknesses ($D = 3$ and $10\,\mathrm{mm}$, respectively).

tional effects arising from the quasi-permanent contact between the oscillating hole at the disk centre and the central rod. Friction introduces a local restriction of the displacement at the disk centre, which is an axisymmetric process. A Green's function is used to embed the point restriction in the SHM which, as expected, only affects the axisymmetric NMV, i.e. $n = 0$. As the trends of discrepancy are similar for all the dominant flexural modes (see figure 3), we conjecture that frictional effects are not the main cause of the model/data discrepancies. The influence of the rod on the motion can therefore be disregarded as it only affects certain modes.

Additional phenomena may be responsible for the observed discrepancy in flexure between theoretical and experimental data and require further analysis to confirm or discard their influence on the motion. In the subsequent sections, we investigate the influence of the edge barrier, stuck along the disk's contour to prevent potential flooding events, on the vibrational behaviour of disk. A viscoelastic disk model is also proposed as an extension of the SHM to account for internal damping.

4. Edge barrier

We devised a technical solution to prevent flooding events that would otherwise disturb the motion of the disk. The barrier is a strip of neoprene foam (synthetic rubber) with rectangular cross-section, which is fixed around the perimeter of each disk (see Part 1 for a complete description). The edge barrier may be seen as an edge stiffener with a given mass, which may potentially modify the vibrational behaviour of the disk.

We have estimated the density of the barrier to be $\rho_b \approx 150\,\mathrm{kg\,m^{-3}}$, the Young's modulus to be $E_b \approx 1\,\mathrm{MPa}$ and Poisson's ratio to be $\nu_b \approx 0.5$, as they are common

values for this material. We denote by h_b and w_b the height and width of the rectangular cross-section, respectively. The following values are used: $h_b = 30\,\mathrm{mm}$ and $w_b = 10\,\mathrm{mm}$ for the 3 mm disk, $h_b = 50\,\mathrm{mm}$ and $w_b = 5\,\mathrm{mm}$ for the 5 mm disk, and $h_b = 50\,\mathrm{mm}$ and $w_b = 10\,\mathrm{mm}$ for the 10 mm disk.

We derive an elastic ring model (see Love 1944) for the edge barrier. The model considers the inertial and elastic properties of the barrier. The ring may be seen as a beam, which is curved at rest, and is referred to as an edge beam in this paper. The vertical motion of the coupled disk/edge beam system is assumed to be unrestricted. The transfer of forces and moments from the edge beam to the disk is modelled in the edge conditions of the disk.

The equations used in the present model were derived by Amon & Dundurs (1968), who solved the coupled disk/beam problem assuming a simply supported or vertically guided beam. The edge-beam model includes the effects of flexure and torsion, in addition to its mass, as these parameters possibly influence the stiffening of the disk edge. Later, Stuart & Carney (1974) considered the vibration problem of an annular plate with a free interior edge beam and a simply supported exterior edge. We follow the approach of Stuart & Carney (1974) for a free edge beam. Neglecting the effects of rotary inertia, the disk's edge conditions are obtained by application of Newton's second law of motion. The force equation is

$$\left\{ -D\partial_r\nabla^2 + \frac{D\,(1-\nu)}{r^2}\left(\frac{1}{r} - \partial_r\right)\partial_\theta^2 + \frac{1}{r^4}\partial_\theta^2\Big[K_b\,(1 - r\partial_r) - F_b\left(\partial_\theta^2 + r\partial_r\right)\Big]\right\}\partial_z\phi^{(\mathrm{i})} = -m_b\omega^2\partial_z\phi^{(\mathrm{i})} \quad (r = R), \tag{4.1a}$$

where L_b is the torsional rigidity, F_b is the beam's flexural rigidity and $m_b = \rho_b h_b w_b$. Likewise, we express the moment equation as

$$\left\{ -D\nabla^2 + \frac{D\,(1-\nu)}{r}\left(\frac{1}{r}\partial_\theta^2 + \partial_r\right) + \frac{1}{r^3}\Big[K_b\,(1 - r\partial_r)\,\partial_\theta^2 + F_b\left(\partial_\theta^2 + r\partial_r\right)\Big]\right\}\partial_z\phi^{(\mathrm{i})} = 0 \quad (r = R). \tag{4.1b}$$

The flexural rigidity of the ring is $F_b = E_b h_b^3 w_b/12(1-\nu_b^2)$. The torsional rigidity linearly maps the angle of twist along the ring to the torque applied. For a rectangular cross-section, Timoshenko & Goodier (1951) derived an exact series expansion in terms of the width to height ratio. We retain the first three terms only and obtain

$$K_b \approx h_b w_b^3\left(\frac{1}{3} - 3.36\frac{w_b}{h_b}\left(1 - \frac{w_b^4}{12h_b^4}\right)\right)G_b, \tag{4.2}$$

where $G_b = E_b/2(1+\nu_b)$ is the shear modulus of the ring. Note that the free edge conditions (2.4) used in §2 are retrieved by setting $K_b = F_b = m_b = 0$.

The solution method requires very little modification to accommodate the new edge conditions (4.1). All that is required is that the eigenfunction expansion for the disk's deflection (2.13) is substituted in (4.1) rather than (2.4).

In order to assess the effects of the edge beam on the response of the disk, we decompose the displacement of the disk with respect to the NMV of the free disk. By using the same basis of NMV to decompose the deflection of the disk, we can compare the RAOs obtained with the edge-beam and free-edge disk models.

Figure 5 shows the flexural modes RAOs for the free-edge and the edge-beam disk models. We show results for $D = 3$ and 10 mm only. The parameters used for the simulations are those specified earlier. Due to uncertainty regarding the values taken for the edge beam parameters, we also examine the sensitivity of the model to the barrier's Young's modulus by generating the RAOs for $E_b = 10$ MPa, i.e. ten times the estimated value.

We observe that the addition of an edge barrier has little effect on the RAOs. In particular, the flexural modes are not affected by the barrier for $E_b = 1$ MPa. However, the RAOs $\tilde{A}_{2,0}$, $\tilde{A}_{3,0}$ and $\tilde{A}_{2,0}$ have slightly increased magnitudes over the frequency range considered, for $E_b = 10$ MPa. It is also seen that the phase shift associated with $\tilde{A}_{2,1}$ is moved towards higher frequencies.

The edge beam (as modelled here) tends to induce modifications in the RAOs that increase the deviation from the experimental data. In results that are not shown here, we also found that the rigid-body modes are less affected by the edge beam than the flexural modes. Therefore, it is reasonable to conjecture that the edge barrier does not affect the response of the disks in our experiments.

5. Extension to the disk model

5.1. *Sensitivity with respect to Young's modulus*

Figure 6 shows the RAOs of $\tilde{A}_{2,0}$ and $\tilde{A}_{0,1}$ for the following values of the Young's modulus: $E = 500$, 838, 1300 and 1600 MPa for $D = 3$ mm, $E = 250$, 503, 750 and 1000 MPa for $D = 5$ mm, and $E = 250$, 496, 750 and 1000 MPa for $D = 10$ mm. We observe that, as the Young's modulus increases, the magnitude of the RAOs decreases, although the qualitative behaviour remains the same. Increasing the Young's modulus stiffens the disk, so that it bends less. Therefore, it is sensible that the amplitudes associated with the flexural modes are lower for higher values of E. The theoretical and experimental RAOs are therefore in better agreement as the Young's modulus is increased.

Furthermore, variations of Young's modulus affect the RAOs more for larger thicknesses, which is a result of the cubic thickness term in the expression of the flexural rigidity. For the 10 mm disk, we obtain a very good agreement between theoretical and experimental RAOs when the Young's modulus is approximately doubled.

Thus far, we have calibrated the SHM with values of the Young's modulus that were measured experimentally by means of four-point bending tests. These values, $E_{\text{exp}} = 838$, 503 and 496 MPa, are significantly smaller than those specified by the manufacturer of the material, $E_{\text{spec}} = 1300$, 750 and 750 MPa, for $D = 3$, 5 and 10 mm, respectively. The model/data comparisons and results of the sensitivity study suggest that the values of Young's modulus used in our model may be inaccurate

Although good repeatability was found during the bending tests (less than 2% relative error as shown by Marsault 2010), it is possible that the tests do not provide a good representation of the bending experienced by the disks in the wave basin experiments. The four-point bending tests consist of loading a parallelepipedic simply supported sample of the material at two points. The load is applied vertically to induce a constant low strain rate, of deflection speed $0.33\,\text{mm}\,\text{s}^{-1}$ (speed at which the load moves and deforms the sample of material). In our hydroelastic experiments, this quantity may be estimated by $2A/T = \text{O}\,(10)\ \text{mm}\,\text{s}^{-1}$, where T is the period of the wave forcing. Therefore, the strain rates involved in our experiments are much higher than those of the bending tests. For a purely elastic material the deflection speed would not have any influence on the value of E but, for viscoelastic materials, the effects of delayed elasticity render the Young's

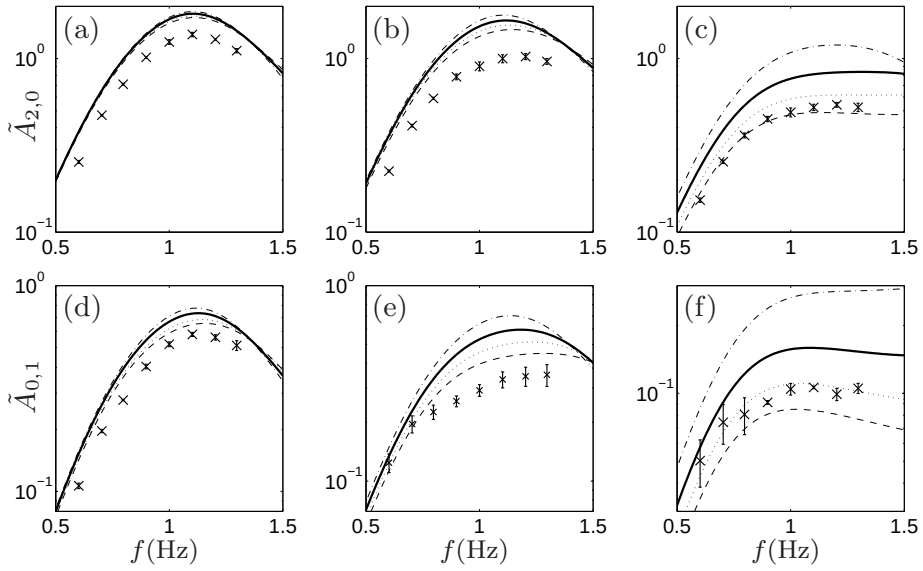

FIGURE 6. Influence of the Young's modulus on the RAOs (a–c) $\tilde{A}_{2,0}$ and (d–f) $\tilde{A}_{0,1}$ for $D = 3\,\text{mm}$ (panels a,d), $D = 5\,\text{mm}$ (panels b,e) and $D = 10\,\text{mm}$ (panels c,f). In each panel, the theoretical RAOs are given for $E = 500, 250, 250\,\text{MPa}$ (dash-dot), $E = 838, 503, 496\,\text{MPa}$ (solid), $E = 1300, 750, 750\,\text{MPa}$ (dot) and $E = 1600, 1000, 1000\,\text{MPa}$ (dash) for $D = 3, 5, 10\,\text{mm}$, respectively.

modulus dependent on the strain rates involved (structure more rigid for higher strain rates), which, in our case, are governed by the deflection speed. In particular, polymeric foams, such as the PVC utilised in the wave basin tests, are known to exhibit linear viscoelastic effects (see, e.g., Altenbach & Eremeyev 2009), which are characterised by lower strain deformations for increased stress rates and increasing strain deformations under sustained load (Flügge 1975).

5.2. *Linear viscoelasticity*

5.2.1. *Model*

For a purely elastic material, Hooke's law is given by

$$\sigma_{ij} = \sigma^v_{ij} + \sigma^d_{ij} = 3K\delta_{ij}\epsilon^v + 2G_s\epsilon^d_{ij}, \tag{5.1}$$

where K and G_s are the bulk and shear moduli, respectively. The components of the stress tensor σ_{ij} are here expressed in terms of the volumetric strain ϵ^v (change of volume at constant shape) and the deviatoric strain ϵ^d_{ij} (change of shape at constant volume). The first and second terms of (5.1) are denoted by σ^v_{ij} and σ^d_{ij}, respectively, corresponding to the volumetric and deviatoric stress components.

We now assume the material is viscoelastic. For small deformations, it is reasonable to consider a linear relation between volumetric stress and strain (Flügge 1975, §8.3). We introduce viscoelasticity in the disk model by describing the deviatoric stress/strain mapping by a standard three-parameter spring/dashpot solid model, composed of a spring (with constant E_0) in series with a Kelvin element, composed of a spring (with constant E_1) and a dashpot (with constant F_1) in parallel. Assuming time-harmonic motion, the

stress/strain mapping is given by

$$\sigma_{ij}^d = \frac{q_0 + \mathrm{i}\omega q_1}{1 + \mathrm{i}\omega p_1}\epsilon_{ij}^d, \tag{5.2a}$$

where

$$p_1 = \frac{F_1}{E_0 + E_1}, \quad q_0 = \frac{E_0 E_1}{E_0 + E_1} \quad \text{and} \quad q_1 = \frac{E_0 F_1}{E_0 + E_1}. \tag{5.2b}$$

The *correspondence principle of viscoelasticity* states that the viscoelastic problem can be formulated as in the purely elastic case, but replacing the elastic constants by their corresponding complex frequency-dependent map (see, e.g., Biot 1955; Flügge 1975). Therefore, the disk equation can be rewritten by substituting $2G_s$ by $(q_0 + \mathrm{i}\omega q_1)/(1 + \mathrm{i}\omega p_1)$. Following Altenbach & Eremeyev (2009), we assume a constant Poisson's ratio, so that only the Young's modulus needs to be replaced by its frequency-dependent viscoelastic counterpart, denoted E^v, which is obtained from the identity $E = 2G_s(1 + \nu)$. We then obtain

$$E^v = \frac{q_0 + \mathrm{i}\omega q_1}{1 + \mathrm{i}\omega p_1}(1 + \nu). \tag{5.3}$$

The boundary value problem described in §2 is now reformulated by replacing the elastic constant β in (2.3) by $\beta^v(\omega) = E^v(\omega)D^3/12\rho_0 g(1 - \nu^2)$. Therefore, the solution method only differs in that the roots of the dispersion relation in the disk-covered fluid region (2.10), denoted by κ_p^v, $p \geq -2$ are all complex. Note that there is a one-to-one correspondence between the roots of the purely elastic and viscoelastic problems. In practice, each κ_p^v is located close to κ_p (in the complex plane), so we use the latter as an initial guess in the dispersion relation solver.

5.2.2. *Calibration*

To estimate the additional parameters (E_0, E_1 and F_1) introduced in the viscoelastic model, we use the data obtained from the four-point bending tests. Although these quasistatic flexural tests are not suitable to measure viscoelastic effects (due to low strain rates and insignificant inertial effects), they allow us to obtain estimates for the parameters. To characterise properly the viscoelastic properties of the PVC used in this work, dynamic tests would be required (Deverge & Jaouen 2004).

The four-point bending tests consist of loading a simply-supported beam vertically and simultaneously at two points, that are equidistant from the mid-point. For a purely elastic material, it is straightforward to obtain a linear mapping $\widetilde{P}(t) = 2G_s w_P(t)$, where w_P is the deflection of the beam at the points at which the load is applied and $\widetilde{P}$ is the scaled load. For a viscoelastic material, the correspondence principle applied in the time domain yields

$$\left(q_0 + q_1\frac{\mathrm{d}}{\mathrm{d}t}\right) w_l = \left(1 + p_1\frac{\mathrm{d}}{\mathrm{d}t}\right)\widetilde{P}. \tag{5.4}$$

The tests were performed with a constant deflection speed, so that $w_l(t) = c_0 t$ with $c_0 \approx 0.33\,\mathrm{mm\,s^{-1}}$. We then obtain a theoretical estimate for the load

$$\widetilde{P}(t) = c_0\left(q_1 - p_1 q_0\right)\left(1 - \mathrm{e}^{-t/p_1}\right) + c_0 q_0 t. \tag{5.5}$$

Note that the system behaves elastically once the exponential term dies out. Therefore, viscoelastic effects influence the response in the early moments only, which is referred to as the viscoelastic regime.

Using the load and deflection data provided by the flexural tests, we estimate the pa-

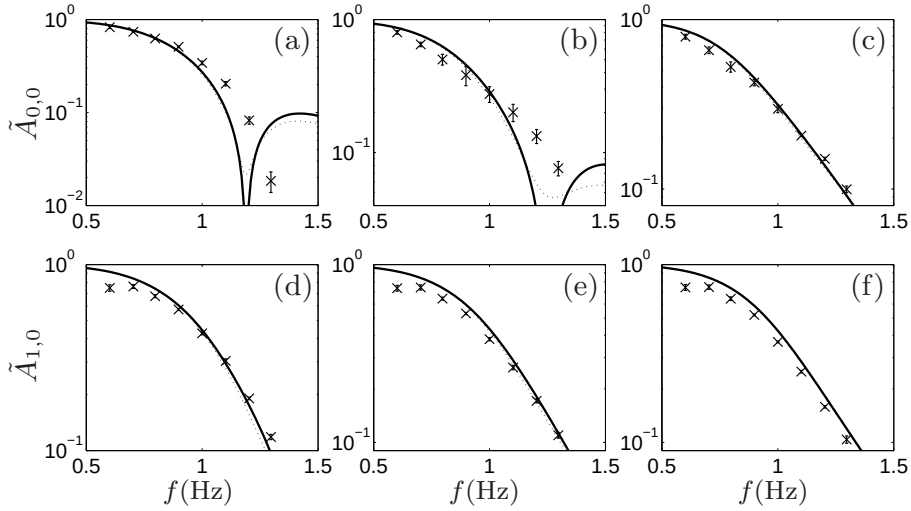

FIGURE 7. Influence of viscoelastic effects on the (a–c) heave and (d–f) pitch RAOs, for $D = 3\,\text{mm}$ (panels a,d) $D = 5\,\text{mm}$ (panels b,e) and $D = 10\,\text{mm}$ (panels c,f). In each panel, the theoretical RAOs are given for the complex Young's modulus E^v (dotted line) and for the purely elastic modulus E (solid line). The experimental RAOs are also given for reference.

rameters q_0, q_1 and p_1, in the least square sense, using a non-linear regression of (5.5). We obtained the following values: $q_0 \approx 587$, 357 and 349 MPa, $q_1 \approx 58.3$, 52.3 and 45.4 MPa s, and $p_1 \approx 433$, 219 and 10.3 μs, for $D = 3$, 5 and 10 mm, respectively. While conducting the calibration analysis, we found an inconsistency between the bending test data and the numerical model in the viscoelastic regime, as the linear theory of viscoelasticity predicts an initial slope larger than the elastic regime slope, i.e. $\widetilde{P}'(0) > c_0 q_0$, which is not respected by the data. This suggests that the experimental data obtained from the four-point bending tests are flawed in the viscoelastic regime. Therefore, the values obtained for the viscoelastic parameters are considered as rough estimates at best, which only allow us to introduce realistic damping effects in the numerical model.

5.2.3. *Results*

We again decompose the deflection of the viscoelastic disk into the NMV of the purely elastic disk. Figure 7 shows the heave and pitch RAOs for the three disk thicknesses. Predictions from the purely elastic and viscoelastic disk models are compared. As expected, viscoelastic effects have little influence on the RAOs of the rigid-body modes. However, in the vicinity of the phase change frequencies for the elastic model (see panels a and b), a non-zero minimum is reached by the viscoelastic model. Therefore, damping effects provide a reasonable explanation to the apparent absence of phase change frequencies in the experimental data.

Figure 8 shows the RAOs associated with the flexural amplitudes $\tilde{A}_{2,0}$ and $\tilde{A}_{0,1}$. We restrict this analysis to two flexural modes for clarity, as, in results not shown here, similar observations for the other dominant flexural modes are made (see Montiel 2012). It is seen that viscoelastic effects become more significant as frequency increases. This is related to the frequency variations $E^v(\omega)$. It can be shown that $|E^v(\omega)| \approx E$ at low frequencies

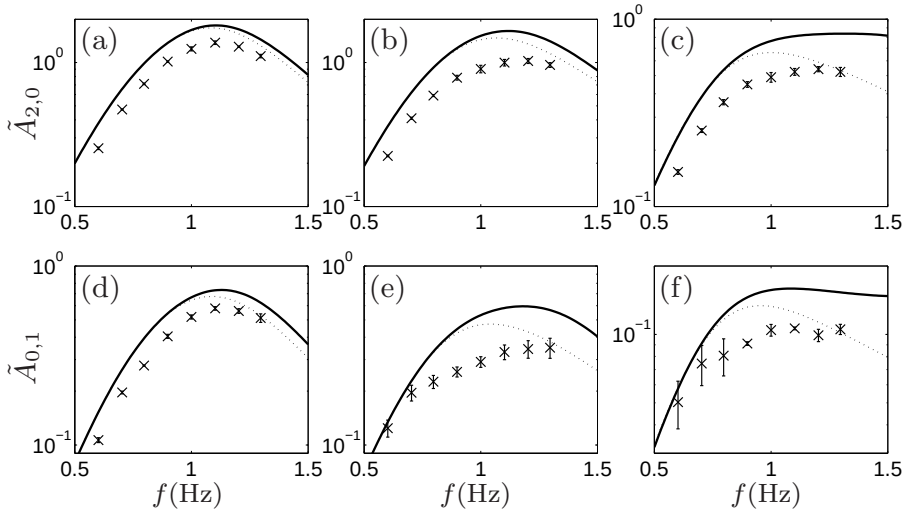

FIGURE 8. As in figure 7 but for the RAOs (a–c) $\tilde{A}_{2,0}$ and (d–f) $\tilde{A}_{0,1}$.

and steadily increases with frequency over the spectrum. Therefore, viscoelastic effects tend to lower the magnitude of the RAOs towards high frequencies.

It is therefore reasonable to conjecture that viscoelastic effects (as modelled here) may explain part of the discrepancy between experimental and theoretical data for the flexural modes at high frequencies. The analysis conducted in this section provides satisfactory results as part of the objectives of the present investigation. Additional dynamic tests would be required to characterise the behaviour of the disks properly and design a model better suited to capture the internal damping in the disks.

6. Modal analysis for the two-disk tests

For the two-disk tests, let s denote the spacing (centre to centre) and ϖ the angle between the incident wave direction and the axis joining the disk centres. We have recorded the deflection of two disks for four different arrangements and two disk thicknesses, $D = 3\,\text{mm}$ and $10\,\text{mm}$. We tested one symmetric arrangement ($\varpi = 0$) for two different spacings $s = 1.88$ and $3\,\text{m}$, and two non-symmetric arrangements ($\varpi = 30°$ and $45°$) with a single spacing $s = 3\,\text{m}$.

We obtain a theoretical solution to the two-disk problem using the interaction theory of Kagemoto & Yue (1986). The method is based on defining the forcing on each disk as the sum of the incident wave forcing and the scattered wavefield from the other disk. The method is theoretically exact in terms of capturing multiple scattering effects.

Using the deflection data allows us to evaluate the amplitudes of the NMV of the two disks. Recall from Part 1 that to define linear time-harmonic quantities from the experimental data, we average the fundamental amplitude of the corresponding time series in a steady-state window, chosen to remove the effects of the transient regime and the reflections from the wave basin's boundaries. For the two-disk tests, our goal is to characterise the effect of the presence of the disks on one another. Therefore, we define the start of the steady-state window after one interaction cycle (i.e. scattered wave

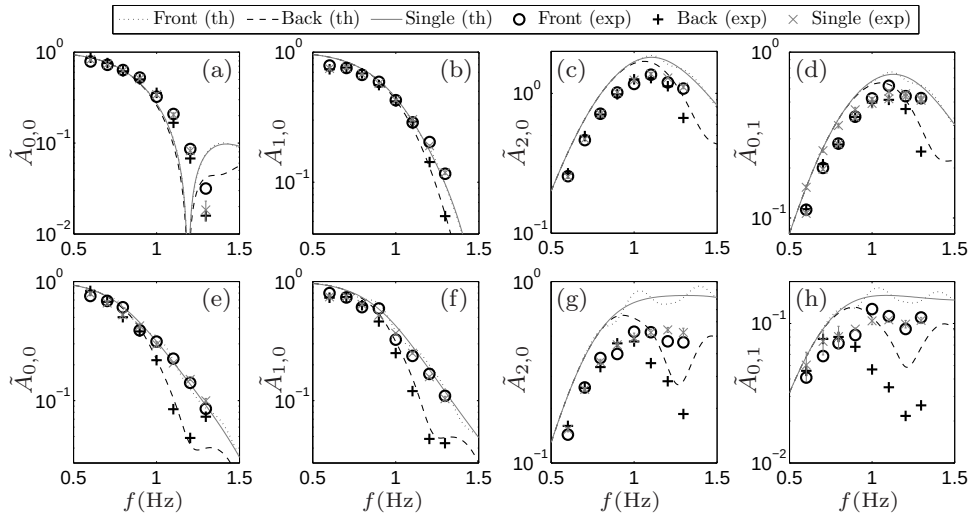

FIGURE 9. Comparison of the theoretical and experimental RAOs of four modes for a symmetric two-disk arrangement with spacing $s = 1.88\,\mathrm{m}$ and disk thickness (a–d) $D = 3\,\mathrm{m}$ and (e–h) $D = 10\,\mathrm{m}$. Results are given for the RAOs (a,e) $\tilde{A}_{0,0}$, (b,f) $\tilde{A}_{1,0}$, (c,g) $\tilde{A}_{2,0}$ and (d,h) $\tilde{A}_{0,1}$. Each panel shows the theoretical and experimental RAOs associated with the front disk (dotted lines and circles, respectively), the back disk (dashed lines and pluses, respectively) and the corresponding single disk (solid lines and crosses, respectively).

travelling from one disk to the other one and back). The proximity of the side walls does not allow us to consider further multiple scattering effects on the response of the system.

6.1. *Symmetric arrangements*

We examine the response of the two symmetric arrangements first, so that we need only consider the symmetric NMV, similarly to the single-disk investigation. We refer to the front and back disks as the closest and furthest disks from the wavemaker in a given arrangement. In addition to analysing the trends of agreement between theoretical and experimental data, we discuss how the RAOs associated with the front and back disks compare to the corresponding single-disk data (with the same thickness parameter). In the following, we present results for four RAOs only, $\tilde{A}_{0,0}$, $\tilde{A}_{1,0}$, $\tilde{A}_{2,0}$ and $\tilde{A}_{0,1}$. The behaviours observed for these amplitudes are indicative of those of all the dominant flexural modes.

Figures 9 and 10 show the RAOs of the four modes considered here for the symmetric arrangements, with spacings $s = 1.88\,\mathrm{m}$ and $3\,\mathrm{m}$, respectively. At low frequencies ($f < 1\,\mathrm{Hz}$ for $D = 3\,\mathrm{mm}$ and $f < 0.8\,\mathrm{Hz}$ for $D = 10\,\mathrm{mm}$), the RAOs associated with the front disk, back disk and single disk coincide for both experimental and theoretical data. The trends of agreement between theory and experiments are therefore similar to those discussed for the single disk in this regime (see §3.2).

For higher frequencies, the experimental and theoretical RAOs provide evidence that the two disks affect each other's motion. In particular, we observe that the RAOs associated with the back disk have lower magnitude than those associated with the front disk. They are characterised by a minimum for most modes. We observe that this minimum is more pronounced for the large spacing than for the small spacing. At high frequencies the presence of the front disk alters the incident wave by scattering, so that the back disk

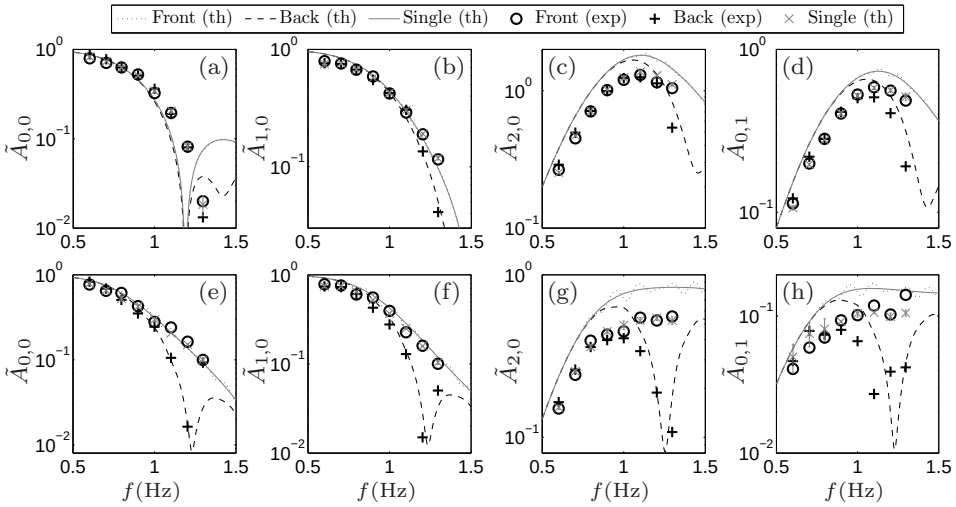

FIGURE 10. As figure 9 but for the large spacing $s = 3\,\mathrm{m}$.

undergoes excitations due to waves with reduced energy. These interaction effects are more significant for the 10 mm disks, as thicker disks more strongly scatter the incident wave. Therefore, we can conclude on the good qualitative agreement between theoretical and experimental RAOs in the high frequency range for both spacings.

To understand how the presence of the back disk affects the front disk's motion, we discuss the theoretical RAOs obtained for the 10 mm disks (see panels e–h). We observe that for each mode, the front disk RAO oscillates about that of the single disk. The 3 mm front disk RAOs show a similar oscillatory behaviour, but of lower magnitude. The maxima of these oscillations (resonances) are associated with the multiple interaction effects of the hydroelastic system. This behaviour is mainly driven by the spacing (see differences between figures 9 and 10), although the properties of the disks also affect the resonances to a lesser extent (differences between $D = 3\,\mathrm{mm}$ and $D = 10\,\mathrm{mm}$). This is consistent with the results of the two-dimensional analysis of Montiel *et al.* (2012*a*), who found that the number of resonances in the reflection coefficient frequency variations increases with the spacing between two floating beams.

We observe a similar oscillatory behaviour in the experimental RAOs, although we do not have a sufficient frequency resolution to show a correspondence of the resonance peaks with those in the theoretical RAOs. As a single interaction cycle was considered in the experiments, we do not expect to observe resonances in the experimental RAOs identical to those in the theoretical RAOs, where multiple interaction effects induce this behaviour. Additional tests in a larger wave basin are required to capture further interactions between the disks once the system is at its steady state without interference from the basin's boundaries.

The oscillations in the front disk remain of low magnitude, even for the 10 mm disks. Therefore, the interaction effects between the two disks are essentially driven by the front disk altering the incident wave so that the motion of the back disk decreases.

The quantitative agreement between the theoretical and experimental RAOs is similar to that estimated for the single disk. In particular, we observe 5–25% relative difference for the rigid-body modes (see panels a,b,e,f), for both front and back disks over the

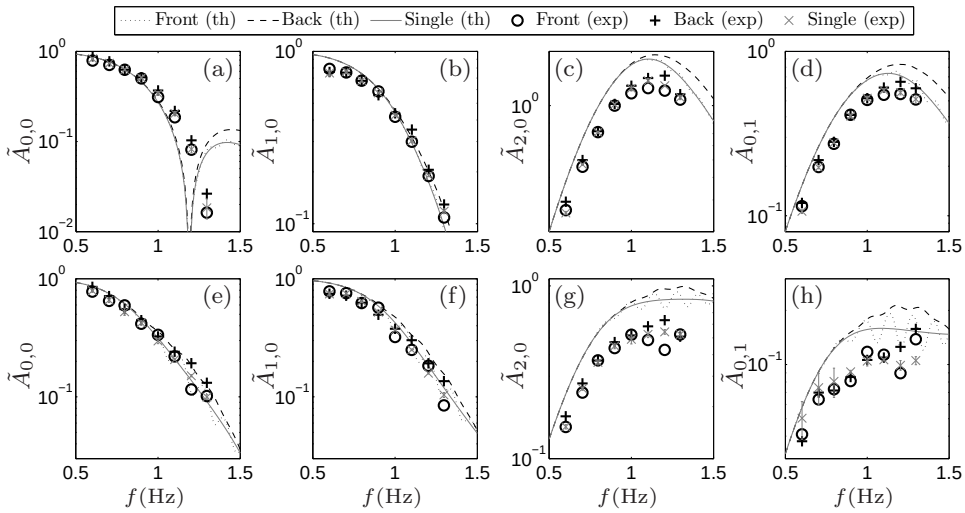

FIGURE 11. As in figure 10 but for an angle $\varpi = 30°$.

frequency range considered here. Similarly to the single-disk analysis, more discrepancy is observed for the flexural modes (see panels c,d,g,h in figures 9 and 10), as we have estimated a relative difference of 30–60%. Therefore, it is logical to conclude that the discrepancies between experimental and theoretical data have the same sources as those observed in the single disk analysis.

6.2. *Non-symmetric arrangements*

For the two non-symmetric arrangements, the asymmetry of the configuration requires that the anti-symmetric NMV are analysed. In results not shown here, we have found that the anti-symmetric RAOs have very low magnitude, and very poor agreement is found between theory and experiments (Montiel 2012). We conjecture that a significant part of the measured amplitudes is due to experimental noise that does not necessarily arise from the asymmetry of the arrangement. To keep the discussion clear and concise, we do not consider these modes in the analysis presented hereinafter.

Figures 11 and 12 show the RAOs for the non-symmetric two-disk arrangement with angles $\varpi = 30°$ and $45°$, respectively. At low frequencies, the theoretical and experimental RAOs of the front and back disks behave as the single disk, similarly to the symmetric case (see §6.1). In addition, we observe an oscillatory behaviour of the theoretical and experimental front disk RAOs about those associated with the single disk, as for the symmetric arrangements. Therefore, the difference in the response of the front disk to that of the single disk is strongly dependent on the spacing parameter but depends very little on the angle.

On the other hand, the response of the back disk differs from that of the symmetric case. Specifically, it is found that the experimental and theoretical RAOs have magnitudes slightly higher than those of the single disk, in the high frequency range. Although the difference with the single-disk response is not large, nor is it negligible.

The response of the back disk is induced by a forcing with an energy higher than that of the incident wave alone. In the present non-symmetric arrangement, the back disk is not

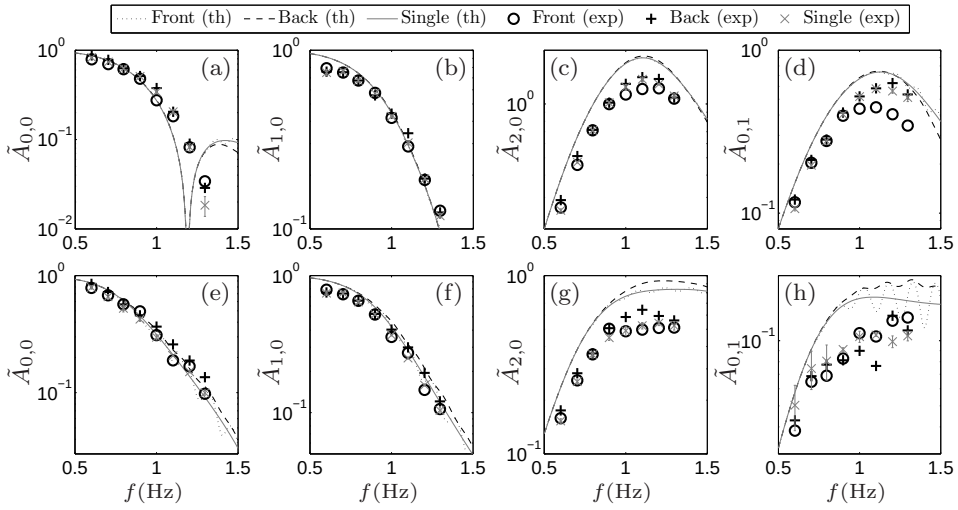

FIGURE 12. As in figure 10 but for an angle $\varpi = 45°$.

hidden behind the front disk in the direction of propagation of the incident wave, so that it is excited by the incident wave that has not been (or has been minimally) altered by the front disk. The second source of excitation comes from the scattered waves produced by the front disk under the incident wave forcing. This phenomenon is already well documented for problems involving multiple bodies and is commonly used to optimise the positioning of arrays of wave energy absorbers (WEAs; see, e.g., Falnes 2002). It is usually characterised by an interaction factor larger than one. The interaction factor is defined as the ratio of the maximum power absorbed by a certain number of interacting WEAs to that absorbed by all these WEAs placed in isolation. In comparison, the RAOs obtained for the symmetric arrangements are characterised by an interaction factor lower than one.

The qualitative agreement between experimental and theoretical data at high frequencies is found to be reasonably good overall. We observe some variability in the experimental data for the 10 mm disks (see panels e–h), so that the partition of energy between the front and back disks is less consistent with the theoretical predictions than for the symmetric arrangement. Quantitatively, the difference between theoretical and experimental data is similar to that found for the single disk.

Overall, we find a good agreement between numerical predictions and experimental data for the symmetric and non-symmetric two-disk tests, suggesting that the interaction theory of multiple scattering used for theoretical predictions is valid in the frequency range considered in the present work.

7. Conclusions

The primary focus of this work has been to validate experimentally a SHM combining thin-elastic plate and potential flow theories, in the framework of the theory of linear water waves. We considered a prototypical problem, that consists of time-harmonic regular wave scattering by one and two floating compliant disks. This is novel experimental

research in that we have characterised (i) the flexural motion of a thin-elastic disk and (ii) the interaction effects on the bending motion when two disks are present. A description and validation of the experimental procedure, designed to reproduce closely the restrictions of the numerical model, are given in Part 1.

An extensive model/experiment comparison was proposed here. We decomposed the motion of the disks into the NMV of the disk *in vacuo* to determine the contribution of the rigid-body modes and the flexural modes separately, for the modes undergoing significant excitation. We analysed the RAOs for the single-disk tests, listed the potential sources of discrepancy between theoretical predictions and experimental data and investigated theoretically the influence of a number of these sources on the response by extension of the standard numerical model.

The main findings of the study conducted for a single disk are as follows.

- The RAOs of the rigid-body modes agree well in the frequency range (5%–20% of pointwise relative difference), except in the vicinity of the theoretical phase change in heave, which is not observed in the experimental data, possibly due to the coarse frequency sampling. The relative difference is largest at low frequencies ($\approx$ 20%) for pitch motion.

- The numerical model overestimates the RAOs of the flexural modes consistently over the frequency range (30%–50% relative difference for the 3 and 10 mm disks, and 40%–70% for the 5 mm disk). The maxima observed for a few flexural modes are in good agreement, and the trends of agreement and discrepancy are consistent for the three thicknesses and for all the modes.

- An analysis of the RAOs at second order allowed us to conjecture that non-linearities are an important source of discrepancy in regimes characterised by modal amplitudes of very low magnitude (e.g. at low frequencies for the flexural modes or in the vicinity of phase change frequencies). This is attributed to the limited resolution of the measuring device. They have minimal importance when the modal amplitudes contribute significantly to the motion.

- The model that includes the edge barrier indicated that the device has little effect on the response of the disk.

- The viscoelastic properties of the disks may explain part of the discrepancy in the flexural modes RAOs at high frequencies, although additional tests are required to characterise the behaviour of the disks properly.

Data comparisons for the response of two disks were also conducted. The RAOs of each disk were compared to the single-disk RAOs, allowing us to determine the influence of the disks on each other's motion. A summary of the outcomes of this analysis is given as follows.

- The front disk behaves similarly to the single disk with additional small-amplitude peaks that arise from the multiple interaction effect in the hydroelastic system. Increasing the spacing between the disks tends to create more peaks in the fixed frequency range. These observations hold for both theoretical and experimental RAOs.

- The motion of the back disk is reduced for symmetric arrangements and increased for non-symmetric arrangements, in comparison to that of the single disk. The energy partition between the front and back disks depends strongly on the combined scattering directional spectrum of the two-disk system, characterised by the interaction factor. These observations hold for both theoretical and experimental RAOs.

- The trends of agreement and discrepancy between theoretical and experimental data are similar to those observed for a single disk. Overall, the qualitative and quantitative agreement of the interaction effects is good for both disks.

The outcomes of the present study (including Part 1) are of primary significance to

sea-ice and VLFS research. We have provided benchmark experimental data for the validation of numerical models used in these fields as the theoretical core of the research to produce more sophisticated models. The experimental method has been proved to be reliable and, therefore, can be reused for other campaigns.

Acknowledgements

The first author FM conducted this research with the support of a University of Otago Doctoral Scholarship.

REFERENCES

Abramowitz, M. & Stegun, I. A. 1970 *Handbook of Mathematical Functions*. Dover.

Allen, J. B. & Rabiner, L. R. 1977 A unified approach to short-time fourier analysis and synthesis. *P. IEEE* **65**, 1558–1564.

Altenbach, H. & Eremeyev, V. A. 2009 On the bending of viscoelastic plates made of polymer foams. *Acta Mech.* **204**, 137–154.

Amon, R. & Dundurs, J. 1968 Circular plate with supported edge-beam. *J. Eng. Mech. Div.-ASCE* **94**, 731–742.

Andrianov, A. I. & Hermans, A. J. 2005 Hydroelasticity of a circular plate on water of finite or infinite depth. *J. Fluids Struct.* **20**, 719–733.

Balmforth, N. J. & Craster, R. V. 1999 Ocean waves and ice sheets. *J. Fluid Mech.* **395**, 89–124.

Bennetts, L. G. 2007 Wave scattering by ice sheets of varying thickness. PhD thesis, University of Reading.

Biot, M. A. 1955 Dynamics of viscoelastic media. In *Proceedings of the Second Midwestern Conference on Solid Mechanics*, pp. 94–108. Purdue University, Lafayette, Indiana.

Chen, X., Wu, Y., Cui, W. & Jensen, J. J. 2006 Review of hydroelasticity theories for global response of marine structures. *Ocean Engng.* **33**, 439–457.

Cohen, L. 1989 Time-frequency distributions–a review. *P. IEEE* **77**, 941–981.

Deverge, M. & Jaouen, L. 2004 A review of experimental methods for the elastic and damping characteristics of acoustical porous materials. In *Proceedings of the 33rd international congress and exposition on noise control engineering, Prague, Czech Republic*.

Falnes, J. 2002 *Ocean Waves and Oscillating Systems: Linear Interactions Including Wave-Energy Extraction*. Cambridge University Press.

Flügge, W. 1975 *Viscoelasticity*, 2nd edn. Springer-Verlag, Berlin.

Fox, C. & Squire, V. A. 1991 Coupling between the ocean and an ice shelf. *Ann. Glaciol.* **15**, 101–108.

Itao, K. & Crandall, S. H. 1979 Natural modes and natural frequencies of uniform, circular, free-edge plates. *J. Appl. Mech.* **46**, 448–453.

Kagemoto, H. & Yue, D. K. P. 1986 Interactions among multiple three-dimensional bodies in water waves: an exact algebraic method. *J. Fluid Mech.* **166**, 189–209.

Kohout, A. L., Meylan, M. H. & Plew, D. R. 2011 Wave attenuation in a marginal ice zone due to the bottom roughness of ice floes. *Ann. Glaciol.* **52**, 118–122.

Kohout, A. L., Meylan, M. H., Sakai, S., Hanai, K., Leman, P. & Brossard, D. 2007 Linear water wave propagation through multiple floating elastic plates of variable properties. *J. Fluids Struct.* **23**, 643–649.

Love, A. E. H. 1944 *A Treatise on the Mathematical Theory of Elasticity*. Dover Publications, New York.

Marsault, P. 2010 Étude des interactions houle/glace de mer. Master's thesis, École Centrale de Nantes (in French).

Meylan, M. H. & Squire, V. A. 1996 Response of a circular ice floe to ocean waves. *J. Geophys. Res.* **101**, 8869–8884.

Montiel, F. 2012 Numerical and experimental analysis of water wave scattering by floating elastic plates. PhD thesis, University of Otago.

Montiel, F., Bennetts, L. G. & Squire, V. A. 2012*a* The transient response of floating elastic plates to wavemaker forcing in two dimensions. *J. Fluids Struct.* **28**, 416–433.

Montiel, F., Bonnefoy, F., Ferrant, P., Bennetts, L. G., Squire, V. A. & Marsault, P. 2012*b* Hydroelastic response of floating elastic disks to regular waves. Part 1: Wave basin experiments. Submitted for publication in J. Fluid Mech.

Peter, M. A., Meylan, M. H. & Chung, H. 2003 Wave scattering by a circular plate in water of finite depth: a closed form solution. In *Proceedings of the 13th International Offshore and Polar Engineering Conference*, pp. 180–185.

Squire, V. A. 2007 Of ocean waves and sea-ice revisited. *Cold Reg. Sci. Technol.* **49**, 110–133.

Squire, V. A. 2011 Past, present and impendent hydroelastic challenges in the polar and subpolar seas. *Philos. T. R. Soc. A* **369**, 2813–2831.

Stuart, R. J. & Carney, J. F. 1974 Vibration of edge reinforced annular plates. *J. Sound Vib.* **35** (1), 23–33.

Timoshenko, S. & Goodier, J. N. 1951 *Theory of Elasticity*. McGraw-Hill, New York.

Watanabe, E., Utsunomiya, T. & Wang, C. M. 2004 Hydroelastic analysis of pontoon-type VLFS: a literature survey. *Eng. Struct.* **26**, 245–256.

Williams, T. D. & Porter, R. 2009 The effect of submergence on the scattering by the interface between two semi-infinite sheets. *J. Fluids Struct.* **25** (5), 777–793.